Cerâmica **68** (2022) 24-32 http://dx.doi.org/10.1590/0366-69132022683853187

X-ray line profile analysis and magnetic and optical properties of $Fe_xZn_{0.95-x}Cr_{0.05}O$ nanoparticles fabricated by sol-gel route

***S. D. Balsure*[1]*, M. Gurav*[2]*, R. H. Kadam*[3]**, K. P. Haval*[4]*, R. M. Tigote*[4]*, A. B. Kadam*[1]**
[1]Jawahar Mahavidyalaya, Department of Physics, Anadur, Osmanabad (M.S.), India
[2]SMP College, Department of Chemistry, Murum, Osmanabad (M.S.), India
[3]Shrikrishna Mahavidyalaya, Materials Science Research Laboratory, Gunjoti (M.S.), India
[4]Dr. Babasaheb Ambedkar Marathwada University, Department of Chemistry, Osmanabad (M.S.), India

Abstract

$Fe_xZn_{0.95-x}Cr_{0.05}O$ nanoparticles have been obtained for the different concentrations of Fe ions by using the sol-gel method. The hexagonal wurtzite structure of all the samples was confirmed by Rietveld refined X-ray diffraction patterns. The addition of Fe ions decreased lattice constants a and c from 3.2487 to 3.2474 Å and 5.2043 to 5.2029 Å, respectively. Uniform deformation, uniform stress deformation, and uniform deformation energy density models were assumed to obtain the crystallite size and strain values from Williamson-Hall analysis. The average crystallite size obtained from all four methods showed increasing variation with the addition of Fe ions in Zn-Cr-O, which was found in good agreement with the Scherrer equation, scanning electron microscopy, and high-resolution transmission electron microscopy results. Energy-dispersive X-ray spectra of typical samples confirmed the stoichiometric proportion of constituent elements. Room temperature ferromagnetism was observed in all the Fe-free and Fe-doped samples. Optical studies were carried out by UV-visible spectrophotometry. The band gap values lay in the range of 3.275 to 3.215 eV.

Keywords: Rietveld refinement, W-H analysis, magnetic properties, optical properties.

INTRODUCTION

Unusual optical, semiconducting, piezoelectric, and sensing properties of ZnO nanoparticles received much attention from scientists and researchers [1-3]. Nanostructured materials with semiconducting behavior are promising candidates for several technological applications [4, 5]. The wide band gap (~3.37 eV), outstanding chemical stability, high excitation binding energy make suitable ZnO nanoparticles for several practical applications in gas sensors, ceramics, optoelectronic devices, field electron emission devices (FED), etc. [6-8]. It has been reported that the size and shape of particles and the introduction of suitable dopants in ZnO crystal can change the structural and optical properties dramatically [9-12]. The addition of transition metal ions like Fe, Mn, Co, Cr, Ni, and Cu in ZnO nanostructures significantly modify the structural, optical, and electrical properties and even the magnetic properties [13-17]. Semiconductors doped with transition metals attract much more attention due to their significant use in lasers with short wavelength, ultraviolet detectors, FET, voltage-dependent resistors, sensors, antibacterial materials, ultrasonic oscillators, etc. [18, 19]. The addition of a fractional amount of transition metals shows diluted magnetic semiconducting behavior and thermal stability decides the desired physical properties which are very useful for practical applications. In concern with the use of dilute magnetic semiconductors (DMSs) in spintronic devices, Fe^{3+} doping is more suitable because Fe^{3+} ion has the same d^5 configuration. Moreover, the lack of nuclear spin stabilizes Fe^{3+} ions more than other transition metal ions [20, 21]. Several synthesis methods have been developed for the fabrication of pure and doped zinc oxide nanoparticles such as chemical co-precipitation [22], combustion synthesis [23], spray pyrolysis [24], hydrothermal [25], thermal plasma [26], sonochemical [27], sol-gel [28], etc. As compared to the other techniques, the sol-gel route produces oxide nanoparticles at a lower cost, shorter time duration, and best control on the shape and size of the particles [29, 30].

Lattice strain and crystallite size are the two main factors that greatly influence the peak broadening, peak intensity, and shifting in Bragg's positions [31]. For the finite size, no crystal shows perfect crystallinity and the intrinsic strain originates due to size confinement increasing the peak widths [24]. Polycrystalline aggregation shows a difference in the crystallite size from particle size [32]. Dislocation density, structure defects, junctions in grain boundaries, contact stress, and stacking faults are the main causes of lattice strain. Crystallite size and lattice strain can be obtained by using X-ray peak profile analysis, which is a powerful averaging method [33]. Several methods have been reported in the literature in order to study the size and strain effects in the crystal lattice, for example, Rietveld refinement, Warren-Averbach analysis, Balzar method, Williamson-Hall (W-H)

---

*ram111612@yahoo.co.in
https://orcid.org/0000-0001-6973-6938

analysis, strain-size plot method, etc. [34]. W-H analysis is the simplest and suitable method to estimate the crystallite size and strain as it uses the full width at half maximum (FWHM) of the diffraction lines.

Our aim is to synthesize the Fe-doped Zn-Cr oxide nanoparticles via sol-gel auto-combustion technique and analyze them by X-ray diffraction, scanning electron microscopy, transmission electron microscopy, Fourier transform infrared spectroscopy, vibrating sample magnetometry, and UV-visible spectrophotometry. Uniform deformation model (UDM), uniform stress deformation model (USDM), and uniform deformation energy density model (UDEDM) were employed for the estimation of crystallite size and lattice strain by using the W-H method. Lorentzian function for size broadening part and Gaussian function for strain broadening part were considered in size-strain plot (SSP) method. A comparative study was carried out for the results obtained from W-H and SSP methods.

MATERIALS AND METHODS

Oxide nanoparticles of $Fe_xZn_{0.95-x}Cr_{0.05}O$ (x= 0, 0.02, 0.04, 0.06, 0.08, and 0.10) were fabricated by using sol-gel auto-combustion method. Metal nitrates (~99.5% pure, A.R. grade) of constituent elements were taken with their weight proportion and mixed with double distilled water. The mixture was stirred continuously and citric acid was added as a chelating agent with the stoichiometric ratio of 1:3. The pH of the solution was maintained at neutral by adding liquid ammonia drop-wise. The whole solution was kept on a hot plate with a magnetic stirrer and heated at a constant temperature of 90 °C. After a couple of hours, the crystal clear solution became viscous and converted into sol and after some time suddenly converted into a gel. Burnt ash powders were obtained by the auto-ignition process of dried gel. Burnt powders were crushed and sintered at an elevated temperature of 850 °C for 6 h in order to obtain the final products. The mole fraction of each element in the obtained materials is given in Table I.

Table I - Elemental molecular mass (g/mol) in $Fe_xZn_{0.95-x}Cr_{0.05}O$ samples.

x	Fe	Zn	Cr	O	Total
0.00	0.000	62.139	2.6	15.999	80.737
0.02	1.117	60.830	2.6	15.999	80.546
0.04	2.234	59.522	2.6	15.999	80.355
0.06	3.351	58.214	2.6	15.999	80.164
0.08	4.468	56.906	2.6	15.999	79.972
0.10	5.585	55.598	2.6	15.999	79.781

X-ray diffraction technique was used to understand the crystallite profile of the as-prepared samples. An X-ray diffractometer (Ultima-IV, Rigaku) was used to record the X-ray diffraction (XRD) patterns with CuKα radiation (λ=1.5405 Å) in the 2θ range of 20° to 80°. All the patterns were recorded at room temperature with a scanning rate of 2 °/min. The surface morphology of the samples was understood by scanning electron microscopy (SEM, JSM-6390LA, Jeol). The stoichiometric proportion of the elements in the composition was analyzed by energy-dispersive X-ray spectroscopy (EDAX). High-resolution transmission electron microscopy (HR-TEM) was used to obtain ultra-high resolution images at an accelerating voltage of 200 kV. Fourier transform infrared spectroscopy (FTIR) was done for the identification of characteristic functional groups present in the samples. All the measurements were performed with a spectrophotometer (IRAffinity-1, Shimadzu) in the wavenumber range of 400 to 4000 cm^{-1}. Magnetic measurements of the powder samples were performed by using a vibrating sample magnetometer (VSM 7404, Lake Shore) with a maximum applied field of 15000 Oe. Optical measurements were carried out by UV-visible spectrophotometry (UV-2102 PCS, Unico).

RESULTS AND DISCUSSION

Rietveld refinement: X-ray diffractograms of as-prepared samples of $Fe_xZn_{0.95-x}Cr_{0.05}O$ refined by Rietveld refinement performed by using FULLPROF software are shown in Fig. 1. All the Bragg's lines were indexed by Miller indices and corresponded to the wurtzite crystal structure. The diffraction patterns were well matched with the international database (COD file 96-900-8878 with space group p63mc). No secondary phase was observed in the XRD patterns suggesting that the Fe ions were incorporated in the Zn-Cr-O wurtzite structure. The goodness factor lay in the range of 1.71 to 2.16 (Fig. 2a), which implied the fitting quality of experimental data. It was also observed that the addition of Fe ions shifted the peak positions slightly towards the higher angles, which in turn reduced the lattice lengths [35]. Fig. 2b shows the variation of lattice constants a and c for Fe-free and Fe-doped Zn-Cr-O nanocrystals. The addition of Fe^{3+} ions in Zn-Cr-O reduced lattice constants a from 3.2487 to 3.2474 Å and c from 5.2043 to 5.2029 Å. The decreasing behavior of lattice parameters a and c can be explained on the basis of ionic radii difference of Fe^{3+} and Zn^{2+} ions. In the present series, Zn^{2+} ions having a larger ionic radius (0.83 Å) [36] were replaced by the Fe^{3+} ions having a relatively smaller ionic radius (0.67 Å) [37], which in turn reduced the lattice spacing. It is worth mentoring here that we considered the electronic state of Fe as Fe^{3+} considering that iron(III) nitrate nonahydrate $[Fe(NO_3)_3.9H_2O]$ was used to prepare the samples. However, the presence of Fe^{3+} should be validated by X-ray photoelectron spectroscopy (XPS).

The well-known Scherrer equation was used to estimate the average particle size by using XRD profiles of the samples [38] and the computed values are given in Table II. The average crystallite size t of the samples was observed in the nanometer range and increased from 17.6 to 23.5 nm with the addition of Fe ions. Similar results of crystallite size for doped zinc oxide were observed in the literature [39, 40]. Moreover, the additional information of

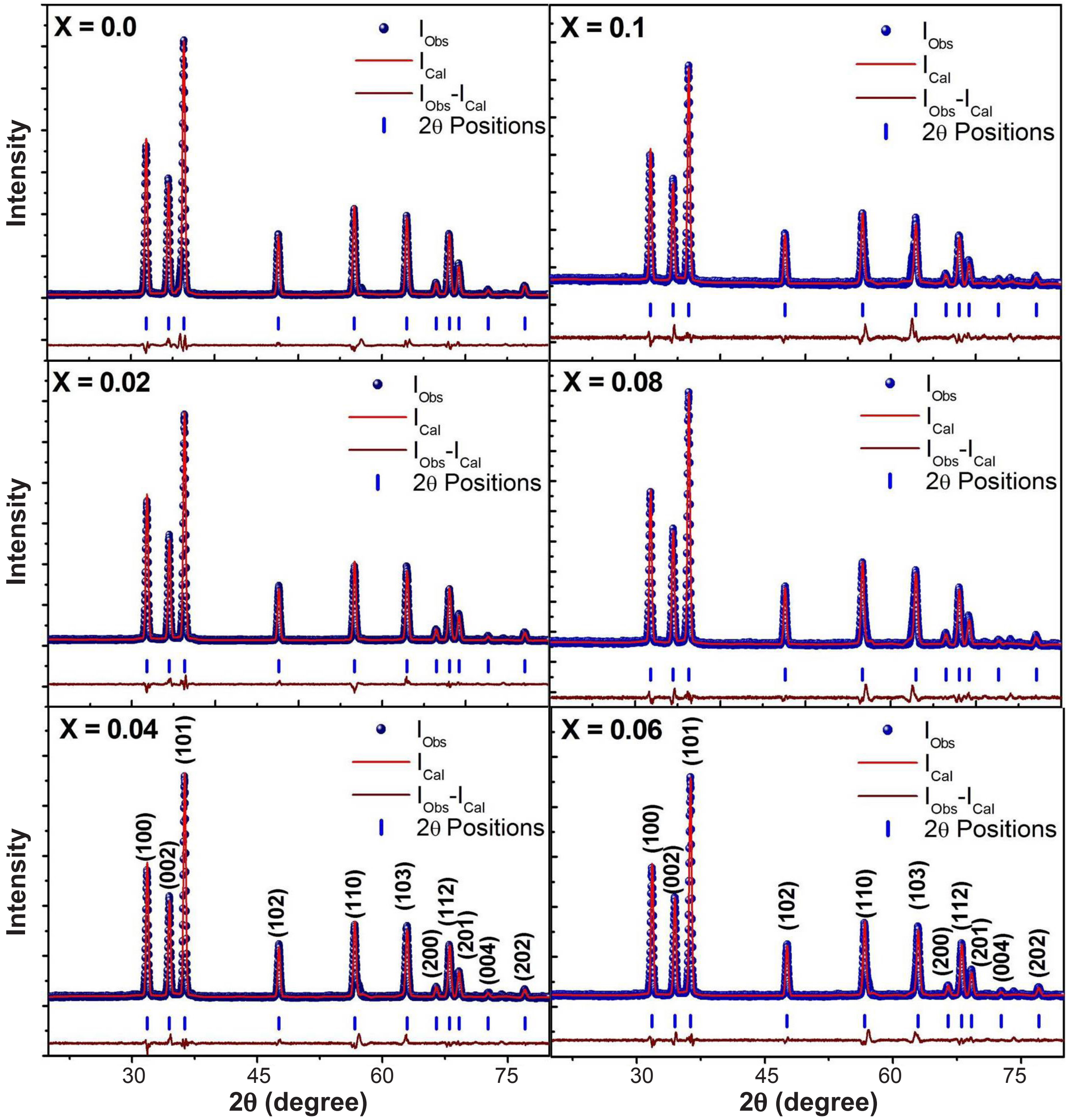

Figure 1: Rietveld refined XRD patterns of $Fe_xZn_{0.95-x}Cr_{0.05}O$ samples.

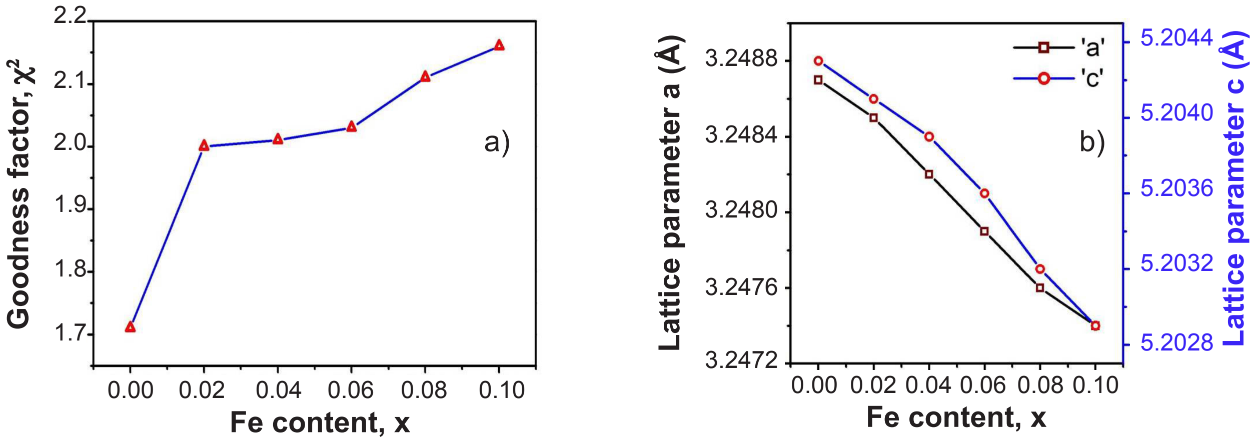

Figure 2: Variation of goodness factor, χ^2 (a), and variation of lattice parameters a and c (b) for $Fe_xZn_{0.95-x}Cr_{0.05}O$.

structural properties due to Fe substitution can be obtained from dislocation density and the strain induced in the crystal lattice [41]. Dislocation density (δ), which can be defined as the number of intercepts by the dislocation lines per unit area in the plane perpendicular to the dislocation lines [42], was computed for all the samples by the following relation [43]:

$$\delta = \frac{1}{t_{D\text{-}S}^2} \quad \text{(A)}$$

where $t_{D\text{-}S}$ is the average crystallite size obtained from the Debye-Scherrer relation. Table II shows that the dislocation density observed for the Fe-free sample was 32.39x10^{14} and reduced to 18.20x10^{14} lines/m^2 with the addition of Fe ions. The decreasing values of δ imply the decrease in lattice imperfections and increase in crystalline quality of the samples. These results are supported by some recent references for Fe substitution [44, 45].

W-H analysis: crystallite size and micro-strain induced in the crystal lattice are mainly related to the broadening of Bragg's peaks [46]. Williamson and Hall suggest a method in which size and strain widths are deconvoluted by using the FWHM as a function of 2θ [47]. By employing the W-H approach, corrected FWHM values were obtained as [48]:

$$\beta_{hkl} = \sqrt{[(\beta_{hkl})_{obs}]^2 - [(\beta_{hkl})_{Instr}]^2} \quad \text{(B)}$$

In addition to the Scherrer equation [38], the strain induced in the crystal lattice follows the following W-H relation [49]:

$$\beta_{hkl}.\cos\theta = \frac{k.\lambda}{t} + 4\varepsilon.\sin\theta \quad \text{(C)}$$

where β_{hkl} is the full width of the peak at half of its maximum height, θ is the peak position, k is a constant, λ is the wavelength (~1.5405 Å), t is the crystallite size, and ε is the micro-strain induced in the crystal lattice. Eq. C is based on the assumption that the crystal is isotropic in nature and hence strain present in the crystal lattice is uniform in all crystallographic directions [50]. In such conditions, Eq. C is referred to as the uniform deformation model (UDM). Plots of 4sinθ versus β.cosθ are shown in Fig. 3. From the slope of UDM plots, strain values were obtained and Y-intercept gave the crystallite diameter. Lattice strain obtained from UDM plots showed positive values and the strain induced in the crystal lattice was of tensile type. The reduction in strain values from 2.35x10^{-4} to 2.98x10^{-4} (Table II) was in accordance with the shrinking of lattice lengths. Crystallite size obtained from the Y-intercept of UDM plots was found in the range of 19.4 to 26.1 nm, which was in good agreement with the Scherrer method.

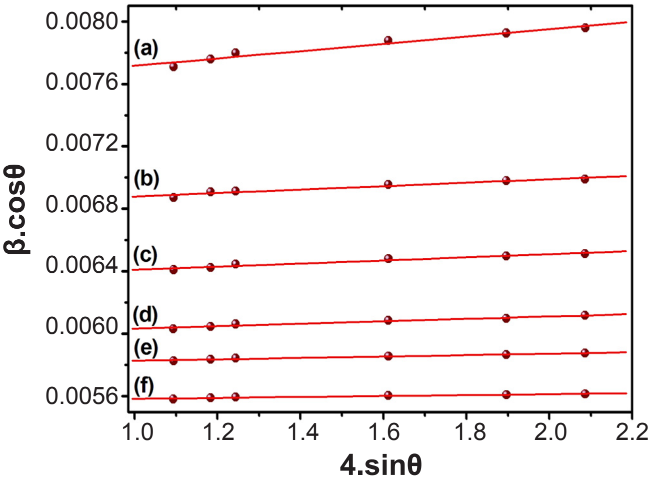

Figure 3: Plots of uniform deformation model for $Fe_xZn_{0.95-x}Cr_{0.05}O$ nanoparticles: a) x=0.0; b) x=0.02; c) x=0.04; d) x=0.06; e) x=0.08; and f) x=0.1.

Similar to the uniform deformation model, the uniform stress deformation model (USDM) is also based on the isotropic nature of the crystals. In this model, according to Hook's law, stress and strain follow the linear proportionality given by the relation σ=Y.ε (where σ is the stress, ε is the strain, and Y is Young's modulus) [22]. According to this model, Eq. C can be modified as:

$$\beta_{hkl}.\cos\theta = \frac{k.\lambda}{t} + \frac{4\sigma.\sin\theta}{Y_{hkl}} \quad \text{(D)}$$

For the material having hexagonal crystal geometry, Young's modulus can be obtained by [51]:

Table II - Crystallite size (t), induced strain (ε), stress (σ), energy density (u), and dislocation density (δ) for Fe-doped $Fe_xZn_{0.95-x}Cr_{0.05}O$ nano-oxides.

x	Scherrer	W-H analysis								SSP method		δx10^{14} (line/m^2)
		UDM		USDM			UDEDM					
	t (nm)	t (nm)	εx10^{-4}	t (nm)	εx10^{-4}	σ (MPa)	t (nm)	εx10^{-4}	u (kJ/m^3)	t (nm)	εx10^{-3}	
0.00	17.57	19.36	2.35	19.28	2.20	27.9	19.33	2.26	3.25	19.32	6.49	32.39
0.02	22.88	21.39	1.10	21.36	1.38	17.5	21.36	1.05	0.70	21.44	4.31	19.10
0.04	23.01	22.95	0.994	22.73	1.01	12.8	22.91	0.959	0.58	22.93	3.79	18.88
0.06	23.20	24.30	0.778	24.30	0.719	9.10	24.30	0.751	0.36	24.27	3.11	18.57
0.08	23.28	25.05	0.455	25.01	0.417	5.28	25.05	0.437	0.12	25.03	2.33	18.45
0.10	23.44	26.09	0.298	26.04	0.298	3.78	26.09	0.287	0.05	26.06	1.90	18.20

$$Y_{hkl} = \frac{\left[h^2 + \frac{(h+2k)^2}{3} + \left(\frac{a}{c}.l\right)^2\right]^2}{S_{11}\left[h^2+\frac{(h+2k)^2}{3}\right]^2 + S_{33}\left(\frac{a}{c}.l\right)^4 + (2S_{13}+S_{44})\left[h^2+\frac{(h+2k)^2}{3}\right]\left(\frac{a}{c}.l\right)^2} \quad (E)$$

where h, k, and l are the Miller indices and the values of electronic compliances S_{11}, S_{13}, S_{33}, and S_{44} are 7.858×10^{-12}, -2.206×10^{-12}, 6.940×10^{-12}, and 23.57×10^{-12} m^2/N, respectively [52]. The average value of Young's modulus estimated for the hexagonal structures of the samples was ~127 GPa, which fairly matched with the literature values for ZnO nanoparticles [24, 46, 50]. The uniform stress observed in the crystal lattice was obtained from the slope of USDM plots (Fig. 4) and crystallite size was estimated from Y-intercept.

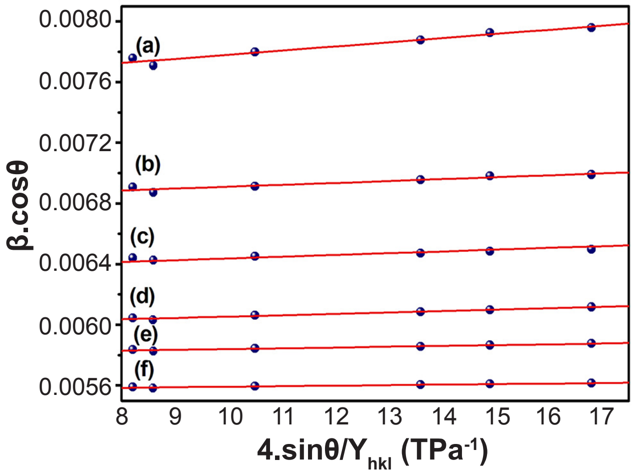

Figure 4: Plots of uniform stress deformation model for $Fe_xZn_{0.95-x}Cr_{0.05}O$ nanoparticles: a) x=0.0; b) x=0.02; c) x=0.04; d) x=0.06; e) x=0.08; and f) x=0.1.

In the case of UDM and USDM, the strain induced in the crystal lattice was assumed to be uniform in all crystallographic directions. Hence the homogeneous isotropic nature of hexagonal crystals was considered where all the properties do not depend on the direction along which they are studied [24]. But in most cases, the uniform distribution of strain in all crystallographic directions cannot be justified. Furthermore, linear proportionality of stress-strain relation is no longer independent while considering the energy density u which can be obtained by $u=\varepsilon^2.Y_{hkl}/2$ and Eq. D can be modified as:

$$\beta_{hkl}.\cos\theta = \frac{k.\lambda}{t} + 4.\sin\theta\left(\frac{2u}{Y_{hkl}}\right)^{1/2} \quad (F)$$

Values of uniform deformation density were obtained from the slope, and the crystallite size was estimated from the Y-intercept of linearly fitted UDEDM (uniform deformation energy density model) lines plotted between $4\sin\theta.(2u/Y_{hkl})^{1/2}$ versus $\beta_{hkl}.\cos\theta$, as shown in Fig. 5. As u is related to the lattice stress by the relation $u=\sigma^2/Y_{hkl}$, the strain can also be calculated. As seen in Table II, crystallite sizes obtained from UDM, USDM, and UDEDM were in good agreement with each other and also with those obtained from the Scherrer method. Also, the strain values showed similar behavior in all cases.

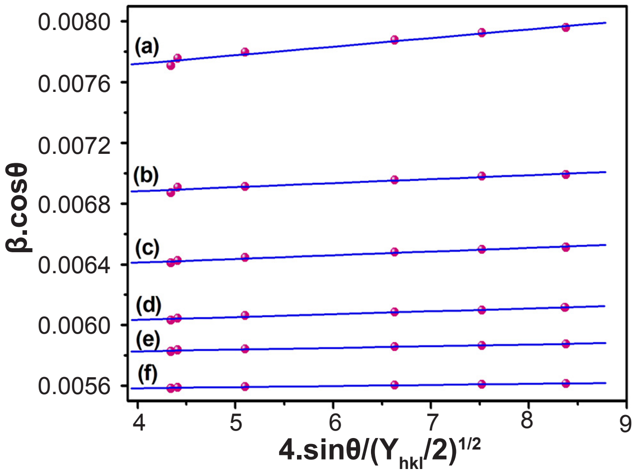

Figure 5: Plots of uniform deformation energy density model for $Fe_xZn_{0.95-x}Cr_{0.05}O$ nanoparticles: a) x=0.0; b) x=0.02; c) x=0.04; d) x=0.06; e) x=0.08; and f) x=0.1.

Size-strain plot method: Williamson-Hall analysis clearly indicated that the isotropic nature of peak broadening is the essential requirement for strain and size estimation. This implies the isotropic nature of diffracting domains due to the micro-strain contribution. Better information of strain-size parameters can be obtained by another method known as size-strain plots (SSP). The main advantage of this method is the minimum importance given to high-angle reflections where the accuracy level is considerably lower. This method is based on the assumption that the estimation of size profile by Lorentzian function and strain profile by Gaussian function can be obtained by following relation [53]:

$$(d_{hkl}.\beta_{hkl}.\cos\theta)^2 = \frac{k.\lambda}{t}(d_{hkl}^2.\beta_{hkl}.\cos\theta) + \left(\frac{\varepsilon}{2}\right)^2 \quad (G)$$

Plots were drawn between $d_{hkl}^2.\beta_{hkl}.\cos\theta$ and $(d_{hkl}.\beta_{hkl}.\cos\theta)^2$ as shown in Fig. 6. Reciprocal of the slopes gave the values of crystallite size t and root mean square values of Y-intercept gave the strain values (Table II).

Surface morphology: field emission scanning electron micrograph of a typical sample (x=0.04) is shown in Fig. 7a. The average grain size was estimated by using software ImageJ and the histogram is presented in the inset of Fig. 7a. SEM image clearly implies that most of the particles were in a spherical shape and the size distribution presented in the histogram indicated the nanoscale dimension of the particles. The average grain size obtained from SEM analysis was closely analog with the results obtained from XRD line profile analysis. Qualitative elemental analysis of the samples was performed by using energy-dispersive X-ray spectroscopy. EDAX spectrum of the typical sample (x=0.04) is shown in Fig. 7b which confirmed the existence of all elements present in the composition. In the

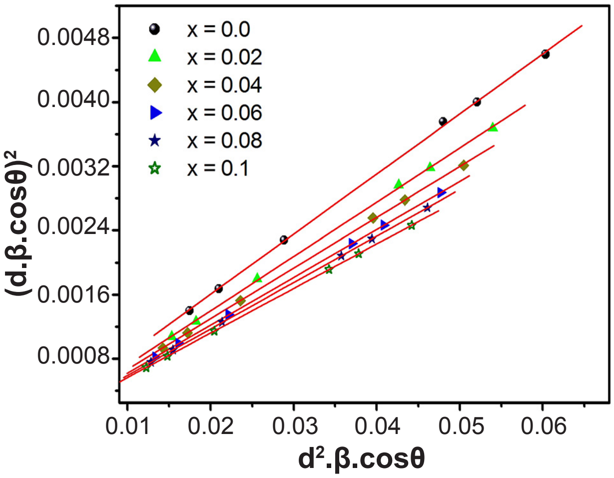

Figure 6: Size-strain plots of $Fe_xZn_{0.95-x}Cr_{0.05}O$ nanoparticles.

EDAX spectrum, three intense peaks were observed nearly at 0.52, 1.01, and 8.64 keV. The peak at 0.52 keV represented the emission of energy from the K-shell of the oxygen atom while the peaks near 1.01 and 8.64 keV represented the emission of energy from Zn [54, 55]. The occurrence of Fe in the composition can be observed by the peaks near 0.72 and 6.4 keV, which indicated that the Fe ions were successfully incorporated in the Zn-Cr-O crystal lattice. The weight percentage observed for all the elements was in accordance with the stoichiometric proportion in the samples. HR-TEM image and SAED (selected area electron diffraction) pattern of the typical sample (x=0.04) is, respectively, shown in Figs. 7c and 7d. Nano-size distribution and low aggregation of the particles were observed in the HR-TEM image (Fig. 7c). The SAED pattern in Fig. 7d shows sharp bright spots, which indicated the polycrystalline nature of the sample with symmetrical orientation. The observed lattice fringes in the HR-TEM image also supported the crystallinity of the sample. The average particle size obtained from the HR-TEM image was found to be 17±5 nm, which was consistent with XRD results.

Fourier transform infrared spectra: FTIR spectra of all the samples were obtained in the wavenumber range of 400 to 4000 cm^{-1} and are represented in Fig. 8. This characterization technique is helpful to identify the functional groups in the material. Four main absorption bands near 1030, 896, 634, and 431 cm^{-1} were observed for all the samples. The peaks observed near 431 and 634 cm^{-1} correspond to the stretching vibrations between zinc and oxygen [56, 57]. Another two peaks near 896 and 1030 cm^{-1} were related to the C-H bending vibrations of the alkene functional group and C-N stretching vibrations of the nitrile functional group, respectively [58, 59].

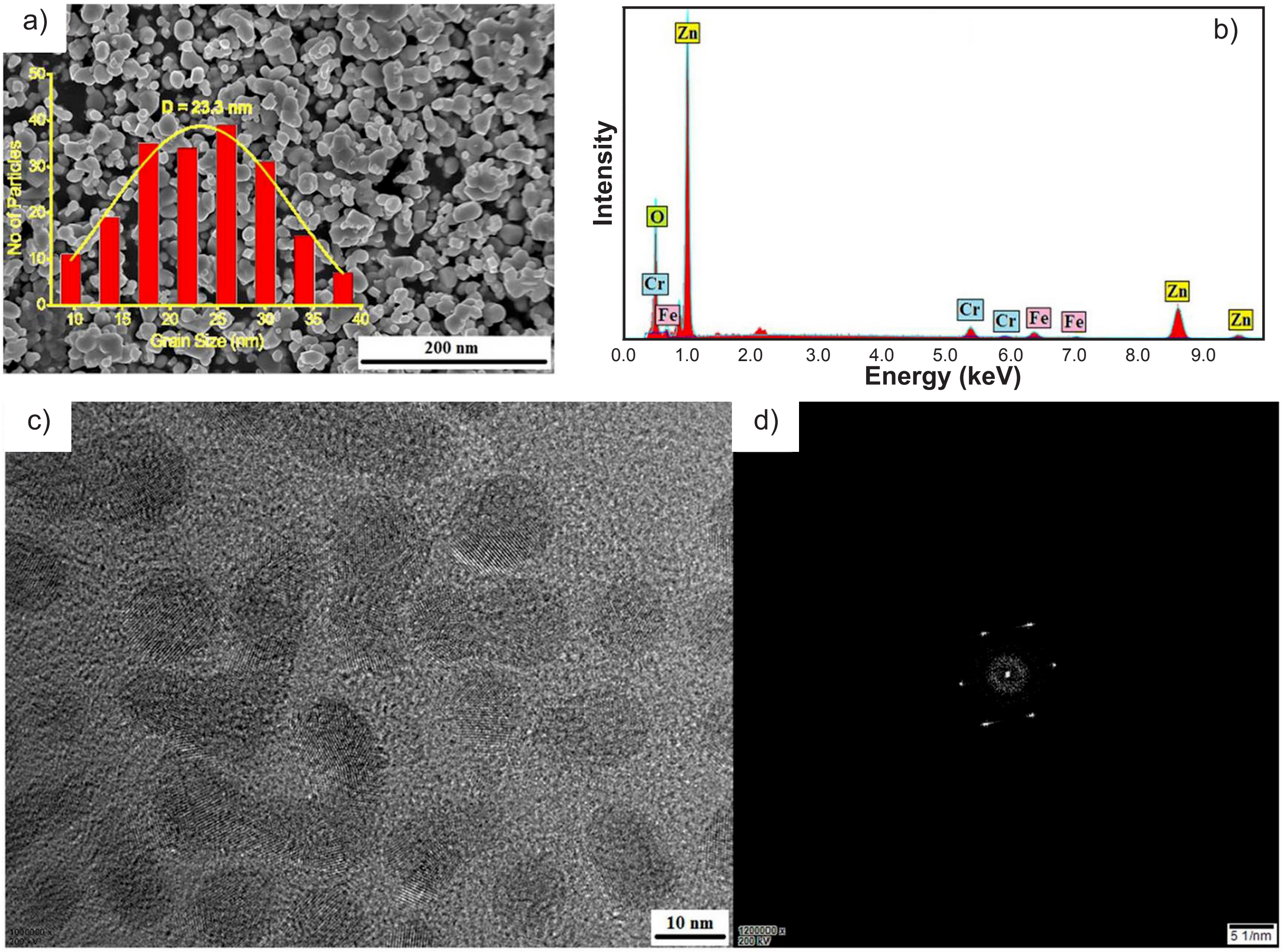

Figure 7: SEM image (a), EDAX spectrum (b), HR-TEM image (c), and SAED pattern (d) of the sample $Fe_{0.04}Zn_{0.91}Cr_{0.05}O$.

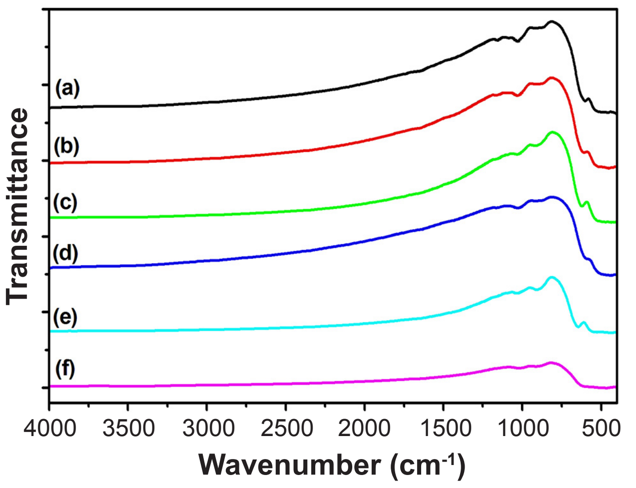

Figure 8: FTIR spectra of $Fe_xZn_{0.95-x}Cr_{0.05}O$ nanoparticles: a) x=0.0; b) x=0.02; c) x=0.04; d) x=0.06; e) x=0.08; and f) x=0.1.

Magnetic properties: Fig. 9 shows the M-H (magnetization versus applied magnetic field) curves of $Fe_xZn_{0.95-x}Cr_{0.05}O$ nanoparticles measured at room temperature. M-H curve clearly showed the intrinsic ferromagnetic properties at room temperature. Noticeable saturation magnetization was observed for the Fe-free sample (x=0.0) with M_S=0.0514 emu/g. The inset of Fig. 9 shows the variation of saturation magnetization with Fe addition in Zn-Cr-O nanoparticles. The increasing percentage of Fe^{3+} ions in Zn-Cr-O nanoparticles increased the saturation magnetization up to x=0.8. Further increase in Fe^{3+} concentration decreased the saturation magnetization up to M_S=0.0965 emu/g. Room temperature ferromagnetic ordering in transition metal (TM)-doped zinc oxides has been proposed by considering several assumptions. Previous studies suggest that the secondary phase, oxygen vacancies, connection between defects and magnetism, etc., play an important role in room temperature ferromagnetic behavior [60-63]. XRD results in the present investigation revealed the formation of a single-phase for all the samples, which in turn ruled out the possibility of ferromagnetism due to secondary phases. Moreover, the considerable reason behind the ferromagnetism in the present samples may be intrinsic. Generally, the intrinsic phenomenon occurs due to exchange interactions [39]. Oxygen-mediated exchange interactions among Fe ions could be responsible for the observed ferromagnetism in Fe-doped Zn-Cr oxides. The doping of Fe ions in Zn-Cr crystal increases the carrier concentration in the form of oxygen vacancies. The higher doping of Fe^{3+} ions enhances the antiferromagnetic interaction between neighboring Fe-Fe ions, resulting in the ferromagnetic behavior. Similar ferromagnetic behavior at higher concentrations of Fe ions was observed in the previous reports [64-67].

Optical properties: optical properties of the Fe-free and doped Zn-Cr oxide nanoparticles were studied by UV-visible diffused reflectance spectroscopy. The band gap energy was estimated by extrapolating the plot between h.ν and α.h.ν by using the following relation [68]:

$$\alpha.h.\nu = (h.\nu - E_g)^n \qquad \text{(H)}$$

where h is the Planck constant, ν is the frequency, α is the

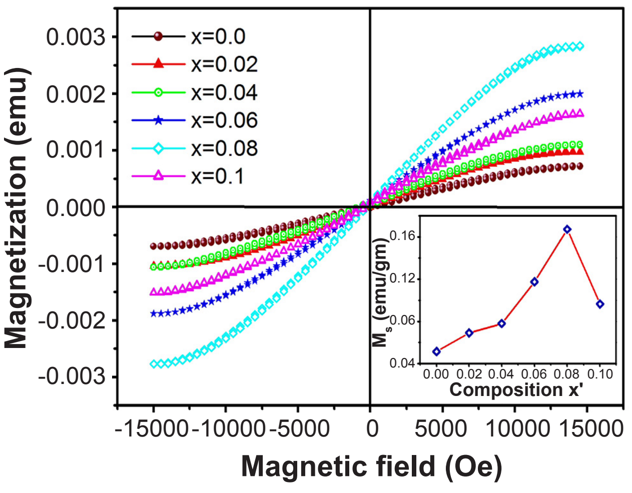

Figure 9: M-H curves of $Fe_xZn_{0.95-x}Cr_{0.05}O$ nanoparticles. Inset shows the variation of saturation magnetization with Fe^{3+} addition in Zn-Cr-O nanoparticles.

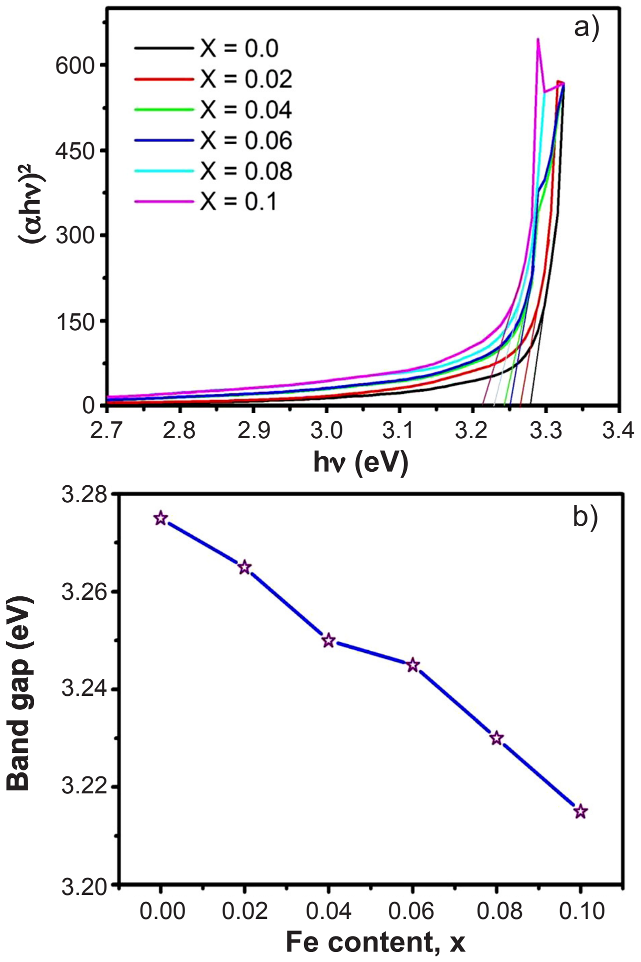

Figure 10: Extrapolated plots of the linear portion of $(\alpha.h.\nu)^2$ versus h.ν (a) and variation of band gap energy with Fe content x (b) in $Fe_xZn_{0.95-x}Cr_{0.05}O$ nanoparticles.

absorption coefficient, and E_g is the band gap energy. The exponential value n depends upon the nature of transitions. For direct transitions, it is 1/2 and for indirect transitions, it is 2 [69]. The values of band gap energy can be obtained from the intercepts on X-axis by extrapolating the linear portion of graphs as shown in Fig 10a. For the undoped $Zn_{0.95}Cr_{0.05}O$ sample (x=0.00), the observed value of band gap energy was 3.275 eV and it slightly decreased with the increasing doping concentration of Fe^{3+} ions (Fig. 10b). Literature review suggests that several factors are responsible for the shrinkage of band gap energy with the substitution of Fe ions in ZnO crystal lattice. According to Sahoo et al. [45], the reduction in band gap with Fe addition is associated with the increasing crystallite size of the samples. Goktas et al. [70, 71] give the reason behind the decreasing band gap, which is related to the sp-d exchange interactions between the band electrons and localized d electrons of Fe replacing the Zn atoms. The decreasing band gap with Fe addition was related to the red shift in the band gap. Bylsma et al. [72] theoretically explained the red shift in the band gap by using second-order perturbation theory. According to this theory, red shift confirmed the uniform substitution of Fe ions in Zn-Cr-O crystal lattice [15].

CONCLUSIONS

Nano-sized particles of Fe-doped Zn-Cr-O wurtzite crystals were successfully obtained by the sol-gel auto-combustion route. Rietveld refined parameters confirmed the phase purity and wurtzite structure of the samples with space group p63mc. The introduction of Fe^{3+} ions reduced the lattice parameters a and c from 3.2487 to 3.2474 Å and 5.2043 to 5.2029 Å, respectively. The nanocrystalline size of all the samples confirmed by UDM, USDM, UDEDM, and SSP methods was found in the range of 17.6 to 26.1 nm. Lattice strain observed in the samples showed positive values indicating the tensile type strain induced in the crystal lattice. The average grain size obtained from SEM micrographs was observed in the range of 19.4 to 24.1 nm, which was analog with the XRD and TEM analysis. Four absorption bands were observed in the FTIR spectra, which identified the stretching vibrations of Zn-O, C-H, and C-N at different wavenumber positions. Noticeable ferromagnetic behavior was observed for all the samples of Fe-doped Zn-Cr-O nanoparticles. The decrease in band gap energy from 3.275 to 3.215 eV noticed the red shift in the band gap.

REFERENCES

[1] Y. Chen, D.M. Bagnall, H.J. Koh, K.T. Park, K. Hiraga, Z. Zhu, T. Yao, J. Appl. Phys. **84** (1998) 3912.

[2] B.J. Jin, S.H. Bae, S.Y. Lee, S. Im, Mater. Sci. Eng. B **71** (2000) 301.

[3] S.W. Chung, J.Y. Yu, J.R. Heath, Appl. Phys. Lett. **76** (2000) 2068.

[4] U. Ozgur, Y.I. Alivov, C. Liu, A. Teke, M.A. Reshchikov, S. Dogan, V. Avrutin, S.J. Cho, H.A. Morkoc, J. Appl. Phys. **98** (2005) 41301.

[5] M. Steinfeldt, A.V. Gleich, U. Petschow, R. Haum, *Nanotechnologies, hazards and resource efficiency*, Springer, Berlin (2007).

[6] S. Hingorani, V. Pillai, P. Kumar, M.S. Multani, Mater. Res. Bull. **28** (1993) 1303.

[7] S. Sakohara, M. Ishida, M. Anderson, J. Phys. Chem. B **102** (1998) 10169.

[8] T. Dippong, E.A. Levei, F. Goga, I. Petean, A. Avram, O. Cadar, J. Sol. Gel. Sci. Techn. **92** (2019) 736.

[9] L. El Mir, J. Lumin. **186** (2017) 98.

[10] J.B. Seol, Y.T. Kim, B.H. Kim, C.G. Park, Metal. Mater. Inter. **22** (2016) 34.

[11] L. El Mir, Z.B. Ayadi, M. Saadoun, H.J. Bardeleben, K. Djessas, A. Zeinert, Phys. Status Solidi A **204** (2007) 3266.

[12] N. Szabo, C. Lee, J. Trimboli, O. Figueroa, R. Ramamoorthy, S. Midlam-Mohler, A. Soliman, H. Verweij, P. Dutta, S. Akbar, J. Mater. Sci. **38** (2003) 239.

[13] D. Kamlakar, S.K. Mandal, R.M. Kadam, P.L. Paulose, A.K. Rajarajan, T.K. Nath, A.K. Das, I. Dasgupta, G.P. Das, Phys. Rev. B **75** (2007) 144404.

[14] J.M.D. Coey, M. Venkatesan, C.B. Fitzgerald, Nat. Mater. **4** (2005) 173.

[15] M. Sajjad, I. Ullah, M.I. Khan, M.Y. Khan, M.T. Qureshi, Res. Phys. **9** (2018) 1301.

[16] D. Bresser, F. Mueller, M. Fiedler, S. Krueger, R. Kloepsch, D. Baither, M. Winter, E. Pillard, S. Passerini, Chem. Mater. **25** (2013) 4977.

[17] B. Allabergenov, S.H. Chung, S.M. Jeong, S. Kim, N. Choi, Opt. Mater. Exp. **3** (2013) 1733.

[18] X.W. Du, Y.S. Fu, J. Sun, X. Han, J. Liu, Semicond. Sci. Technol. **21** (2006) 1202.

[19] T. Dippong, E.A. Levei, C.L. Lengauer, A. Daniel, D. Toloman, O. Cadar, Mater. Charact. **163** (2020) 110268.

[20] S.T. Ochsenbein, D.R. Gamelin, Nat. Nanotechnol. **6** (2011) 112.

[21] J. Tribollet, J. Behrends, K. Lips, EPL **84** (2008) 20009.

[22] A. Aimable, M.T. Buscaglia, V. Buscaglia, P. Bowen, J. Eur. Ceram. Soc. **30** (2010) 591.

[23] N.R. Noori, R. Mamoory, P. Alizadeh, A. Mehdikhani, J. Ceram. Process. Res. **9** (2008) 246.

[24] A.K. Zak, W.H. Majid, M.E. Abrishami, R. Yousefi, Solid State Sci. **13** (2011) 251.

[25] W. Bai, W.F. Xu, J. Wu, J.Y. Zhu, G. Chen, J. Yang, T. Lin, X.J. Meng, X.D. Tang, Physica E Low Dimens. Syst. Nanostruct. **40** (2008) 822.

[26] T.S. Ko, S. Yang, H.C. Hsu, C.P. Chu, H.F. Lin, Mater. Sci. Eng. B **134** (2006) 54.

[27] M.R Vaezi, S.K. Sadrnezhaad, Mater. Des. **28** (2007) 515.

[28] S.R. Wadgane, S.T. Alone, A. Karim, G. Vats, S.E. Shirsah, R.H. Kadam, J. Magn. Magn. Mater. **471** (2019) 388.

[29] K.H. Mabhouti, M. Karamirad, P. Norouzzadeh, M.M. Golzan, R. Naderali, J. Elect. Mater. **49** (2020) 3668.

[30] T. Dippong, I.G. Deac, O. Cadar, E.A. Levei, I. Petean, Mater. Charact. **163** (2020) 110248.

[31] H. Irfan, M. Racik, S. Anand, J. Asian Ceram. Soc. **6** (2018) 54.
[32] K. Ramakanth, *Basic of diffraction and its application*, I.K. Int. Publ., New Delhi (2007).
[33] H.M. Rietveld, Acta Crystallogr. **22** (1976) 151.
[34] B.E. Warren, B.L. Averbach, J. App. Phys. **21** (1950) 595.
[35] B.R. Kumar, B. Hymavathi, J. Asian Ceram. Soc. **5** (2017) 94.
[36] T. Tatrachuk, M. Bououdina, W. Macyk, O. Shyichuk, N. Paliychuk, I. Yaremiy, B. Al-Najar, M. Pacia, Nanoscale Res. Lett. **12** (2017) 141.
[37] R.H. Kadam, A.R. Biradar, M.L. Mane, S.E. Shirsath, J. Appl. Phys. **112** (2012) 43902.
[38] R.H. Kadam, K. Desai, V.S. Shinde, M. Hshim, S.E. Shirsath, J. Alloys Compd. **657** (2016) 487.
[39] S.B. Rana, R.P. Singh, J. Mater. Sci. Mater. Electron. **27** (2016) 9346.
[40] N. Sharma, S. Jandaik, S. Kumar, M. Chitkara, I.S. Sandhu, J. Exp. Nanosci. **11** (2016) 1.
[41] S. Roy, M.P. Ghosh, S. Mukherjee, Appl. Phys. A **127** (2021) 451.
[42] B. Yahmadi, O. Kamoun, B. Alhalaili, S. Alleg, R. Vidu, N.K. Turki, Nanomaterials **10** (2020) 1507.
[43] A. Goktas, A. Tumbul, Z. Aba, A. Kilic, F. Aslan, Opt. Mater. **107** (2020) 110073.
[44] E. Nurfani, A. Lailani, W.A.P. Kesuma, M.S. Anrokhi, G.T.M. Kadja, M. Rozana, Opt. Mater. **112** (2021) 110768.
[45] B. Sahoo, S.K. Pradhan, D.K. Mishra, S.K. Sahoo, R.R. Nayak, D. Behera, Optik **228** (2021) 166134.
[46] B.R. Kumar, B. Hymavathi, Adv. Nat. Sci. Nanosci. Nanotechnol. **9** (2018) 35018.
[47] P. Bindu, T. Sabu, J. Theor. Appl. Phys. **8** (2014) 123.
[48] V. Biju, N. Sugathan, V. Vrinda, S.L. Salini, J. Mater. Sci. **43** (2008) 1175.
[49] R.H. Kadam, R.B. Borade, M.L. Mane, D.R. Mane, K.M. Batoo, S.E. Shirsath, RSC Adv. **10** (2020) 27911.
[50] V.T. Prabhu, K.V. Rao, V.S. Kumar, B.S. Kumari, World J. Nano Sci. Eng. **4** (2014) 21.
[51] J.F. Nye, *Physical properties of crystals: their representation by tensor and matrices*, Oxford, New York (1985).
[52] J.M. Zhang, Y. Zhang, K.W. Xu, V. Ji, Solid State Commun. **139** (2006) 87.
[53] M. Rabie, A. Palevicius, A. Monshi, A. Nasiri, A. Vikausakas, G. Janusas, Nanomaterials **10** (2020) 1.
[54] R. Kumari, A. Sahil, N. Goswami, Prog. Nat. Sci. Mater. Int. **25** (2015) 300.
[55] A. Sahai, N. Goswami, Ceram. Int. **40** (2014) 14569.
[56] R. Waheb, S.G. Ansari, Y.S. Kim, M. Song, H.S. Shin, Appl. Surf. Sci. **255** (2009) 4891.
[57] N. Goswami, A. Sahai, Mater. Res. Bull. **48** (2013) 346.
[58] W. Muhammad, N. Ullah, M. Haroon, B.H. Abbbasi, RSC Adv. **9** (2019) 29541.
[59] J.S. Kumar, S.V. Kumar, S.R. Kumar, Res. Eff. Technol. **3** (2017) 459.
[60] D. Guruvammal, S. Selvaraj, S.M. Sundar, J. Magn. Magn. Mater. **452** (2018) 335.
[61] A. Goktas, I.H. Mutlu, Y. Yamada, E. Celik, J. Alloys Compd. **553** (2013) 259.
[62] A. Goktas, F. Aslan, B. Yesilata, I. Boz, Mater. Sci. Sem. Proc. **75** (2018) 221.
[63] D.E. Aimouch, S. Meskine, A. Boukortt, A. Zaoui, J. Magn. Magn. Mater. **451** (2018) 70.
[64] P.K. Sharma, R.K. Dutta, A.C. Pandey, S. Layek, H.C. Verma, J. Magn. Magn. Mater. **321** (2009) 2587.
[65] T. Dippong, O. Cadar, I.G. Deac, M. Lazar, G. Borodi, E.A. Levei, J. Alloys Compd. **828** (2020) 154409.
[66] C. Liu, D. Meng, X. Pang, X. Wu, J. Xie, X. Yu, L. Chen, X. Liu, J. Magn. Magn. Mater. **324** (2012) 3356.
[67] T. Dippong, E.A. Levei, I.G. Deac, F. Goga, O. Cadar, J. Anal. Appl. Pyrol. **144** (2019) 104713
[68] G.N. Narayanan, R.S. Ganesh, A. Karthigeyan, Thin Solid Films **598** (2016) 39.
[69] M. Goswami, N.C. Adhikary, S. Bhattacharjee, Optik **158** (2018) 1006.
[70] A. Goktas, A. Tumbul, F. Aslan, J. Sol. Gel. Sci. Technol. **90** (2019) 487.
[71] A. Goktas, J. Alloys Compd. **735** (2018) 2038.
[72] R.B. Bylsma, W.M. Becker, J. Kossut, U. Debska, D.Y. Short, Phys. Rev. B **33** (1986) 8207.

(Rec. 06/06/2021, Rev. 19/07/2021, 03/08/2021, Ac. 12/08/2021)